# A Unified Virtual Power Decoupling Method for Droop-Controlled Parallel Inverters in Microgrids

Teng Wu, *Student Member, IEEE*, Zeng Liu, *Member, IEEE*, Jinjun Liu, *Senior Member, IEEE*, Shike Wang, and Zhiyuan You

***Abstract*—The coupling between the active and the reactive power of the droop-controlled inverter is critical in the low-voltage microgrid. The conventional virtual power-based control strategy can decouple the active and the reactive power of the inverter, whereas the active power of the load is probably not equally shared among the parallel inverters in the microgrid. To tackle this issue, this paper proposes an improved virtual power-based control method for the droop-controlled parallel inverters with a unified rotation angle in the power transformation. Meanwhile, the optimal value of the unified rotation angle is rigorously derived through investigating the relative stability of the system by innovatively adopting Routh Stability Criterion. Moreover, the proposed method is enhanced by introducing low-pass filters in the coupling path for further mitigating the coupling between the active and the reactive power of the inverter. Additionally, the stability analysis and parameter design for the proposed method are comprehensively presented. Finally, the effectiveness of the proposed method is validated by the simulation and experimental results.**

***Index Terms*—Droop control, microgrid, parallel inverters, power decoupling, virtual power.**

## I. Introduction

MICROGRID is an integrated energy system consisting of interconnected loads and distributed generations (DGs) [1]–[6], which are usually linked to a common bus through power electronic interfaces like inverters [2], [7], [8]. The inverters are controlled coordinately to realize power sharing among DGs. In a microgrid where communication lines are not suitable for information exchanges due to the distributed physical locations or to the noises along the lines, a better choice for the coordinative control of parallel inverters is usually the frequency- and voltage-droop control method, which is based on the condition of the line impedance being mainly inductive [9], [10]. Generally, this condition is available in a high- or medium-voltage microgrid where the line impedance ratio R/X is small enough that the line impedance could be regarded as mainly inductive [11], [12], [25]. However, in a low-voltage microgrid, the condition for the conventional droop control is no longer available due to the high R/X ratio of line impedance, which could result in coupling between the active and the reactive power and, thus, deteriorates dynamic response and system stability [11], [13].

In order to deal with the above problem in the low-voltage microgrid, a number of improved droop control methods were proposed to decouple the active and the reactive power of the inverter, which can mainly be divided into three categories: virtual impedance-based [14]–[18], [26], virtual power-based [19], [27], and virtual frequency- and voltage-based decoupling method [11]. The virtual impedance-based control method is widely used for dealing with the above problem in the low-voltage microgrid [14]–[18], [26]. In this method, a virtual impedance loop is implemented to modify the equivalent output impedance of the inverter to be predominantly inductive. However, it is a challenging issue to design the virtual impedance value with a least possible complexity which can effectively decouple the power flows and at the same time, can maintain good system dynamics and stability [19]. The virtual power-based control scheme is also widely recognized, which could decouple the power flows by rotating the power vectors with the impedance angle [19], [27]. The virtual active and reactive power is respectively related to the frequency and voltage amplitude without coupling each other. Droop control is adopted in the virtual frame to ensure the virtual power being shared. However, this method cannot guarantee the sharing of actual power if the distribution line impedance angles of each DG are different. The virtual frequency- and voltage-based decoupling method is an analog of the virtual power-based decoupling method [11]. The frequency and the voltage amplitude are transformed into the virtual frame to build a new relationship with, respectively, the active and the reactive power. However, this paper does not provide a mathematical derivation to prove that the power flows are decoupled in the virtual frequency and voltage frame.

Among these three existing types of decoupling method for parallel inverters in microgrid, the virtual power-based method is attractive because of simple design process and clear physical meaning. In this method, the virtual power is adopted directly in the droop control, which can be shared among parallel inverters. The transformation from the virtual power to the actual power depends on the impedance angle of the inverter transmission line which could be different among the inverters, and the actual power may not be shared equally. Therefore, the main issue of the virtual power-based method is that the actual power sharing performance heavily relies on the consistence of line impedance angles of the inverters.

Manuscript received February 26, 2015; revised July 3, 2015 and September 17, 2015; accepted October 21, 2015. Date of publication November 4, 2015; date of current version March 2, 2016. This work was supported by the National Natural Science Foundation of China under Grant 51437007, and the Power Electronics Science and Education Development Program of Delta Environmental and Educational Foundation under Grant DREM2014002. Recommended for publication by Associate Editor Y. W. Li.

The authors are with the State Key Lab of Electrical Insulation and Power Equipment, School of Electrical Engineering, Xi'an Jiaotong University, Xi'an 710049, China (e-mail: wuteng008@yeah.net; zeng.liu@ieee.org; jjliu@mail.xjtu.edu.cn).

Color versions of one or more of the figures in this paper are available online at http://ieeexplore.ieee.org.

Digital Object Identifier 10.1109/TPEL.2015.2497972

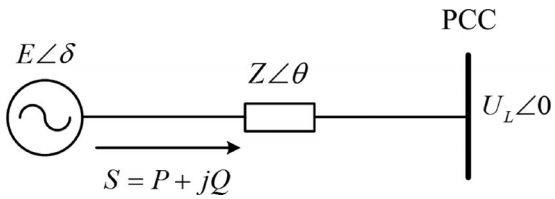


Fig. 1. Equivalent circuit of an inverter connected to the ac bus of the microgrid.

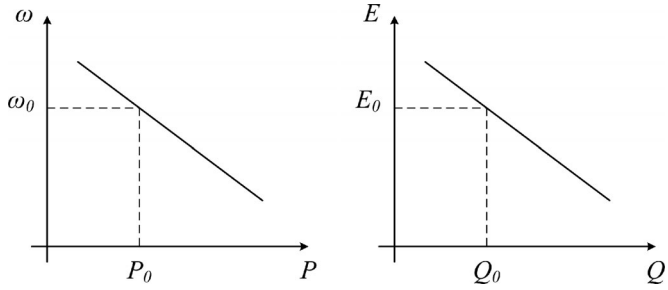


Fig. 2. Traditional frequency and voltage droop characteristics.

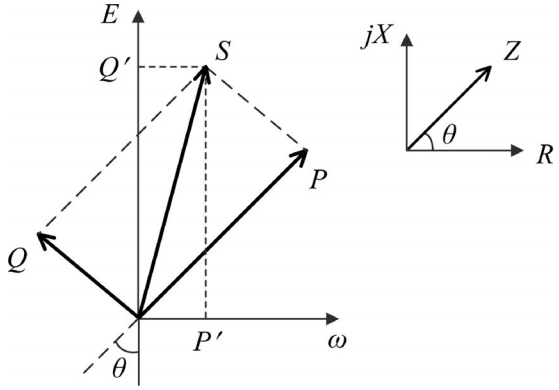


Fig. 3. Conventional virtual power-based decoupling.

This paper tries to solve this problem by utilizing a unified transformation from the virtual power to the actual power for parallel inverters in the microgrid. Compared with the existing decoupling methods, the contribution of this paper can be concluded into three points. First, the virtual power-based control utilizing a unified power transformation is proposed, and the value of the unified rotation angle in the power transformation is optimized. Therefore, the actual power will be shared equally as long as the virtual power is evenly shared among parallel inverters, while the coupling between the active and the reactive power of the inverter can be mitigated for a better system dynamic and stability performance, and thus, the limitation of the conventional virtual power-based control can be overcome. Meanwhile, the optimal value of the unified rotation angle is rigorously derived through investigating the relative stability of the system by innovatively adopting Routh Stability Criterion, and this is seldom mentioned in [11]. Second, the proposed control method is enhanced by introducing the low-pass filters (LPFs) in the coupling path of the system, which can further mitigate the coupling between the active and the reactive power, while the power sharing performance will not be influenced. Third, the stability of the system is comprehensively analyzed, which is significant for the design of essential parameters in the proposed control scheme.

The rest of this paper is organized as follows. The conventional virtual power-based control method is briefly reviewed in Section II. The small-signal model and the determination of the optimal rotation angle are presented in Section III. Subsequently, the proposed unified virtual power method is further improved in Section IV. Furthermore, Section V provides the stability analysis and parameter design for the proposed method. Simulation and experimental results are presented respectively in Sections VI and VII to verify the effectiveness of the proposed method. Finally, the concluding remarks are given in Section VIII.

## II. Conventional Virtual Power-Based Control Method

For an ac system with a given distribution line impedance, the active and the reactive power flows between two voltages $E\angle\phi$ and $U_L\angle 0$ shown in Fig. 1 obey the following relationship:

$$P = \frac{EU_L\sin\phi}{Z}\sin\theta + \frac{E\left(E - U_L\cos\phi\right)}{Z}\cos\theta \tag{1}$$

$$Q = -\frac{EU_L\sin\phi}{Z}\cos\theta + \frac{E\left(E - U_L\cos\phi\right)}{Z}\sin\theta \tag{2}$$

where $E$ and $U_L$ are, respectively, the DG's output terminal voltage and the PCC voltage, and $\phi$ is the phase angle difference between $E$ and $U_L$, and $Z\angle\theta$ denotes the distribution line impedance.

In an HV or MV microgrid, the line impedance is considered to be inductive ($\theta = 90^\circ$) due to the typically high inductive components of the line and the inductor filter. In addition, the phase angle difference $\phi$ is usually quite small. Therefore, (1) and (2) can be simplified by regarding that $\sin\phi \approx \phi$ and $\cos\phi \approx 1$ [3], [10], [21]

$$P \approx \frac{EU_L\phi}{Z} \tag{3}$$

$$Q \approx \frac{E\left(E - U_L\right)}{Z}. \tag{4}$$

Such relationships in (3) and (4) lay the foundation of the active power-frequency and the reactive power-voltage amplitude droop characteristics [3], [10], [21], which are illustrated in Fig. 2 and mathematically expressed as

$$\omega^* = \omega_0 - m\left(P - P_0\right) \tag{5}$$

$$E^* = E_0 - n\left(Q - Q_0\right) \tag{6}$$

where $\omega^*$ and $E^*$ are the generated reference of frequency and voltage amplitude. $P$ and $Q$ are the measured output active and reactive power. $\omega_0$ and $E_0$ are the rated voltage frequency and amplitude, while $P_0$ and $Q_0$ are, respectively, the dispatched active and reactive power at the frequency $\omega_0$ and voltage amplitude $E_0$. $m$ and $n$ (defined as positive) are the slopes of the $P$-$\omega$ and $Q$-$E$ droop characteristics.

However, in an LV microgrid, the conventional droop method suffers from the active and reactive power coupling, which could lead to system stability concerns. To achieve power decoupling,

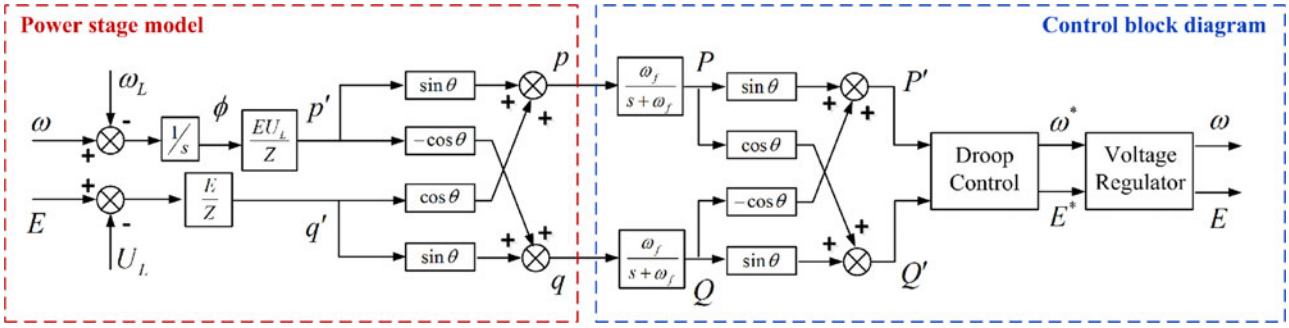


Fig. 4. Block diagram of the conventional virtual power-based decoupling method.

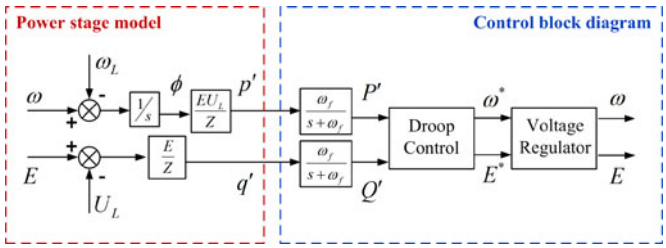


Fig. 5. Block diagram of the decoupled system.

a control strategy based on virtual power was proposed in [19]. The virtual active and reactive power ($P'$ and $Q'$) are obtained by using an orthogonal rotating transformation matrix $\boldsymbol{T}$ to rotate the active and the reactive power vectors by the impedance angle $\theta$, which is shown in Fig. 3 and expressed in (7). The block diagram of the conventional virtual power decoupling method is illustrated in Fig. 4, where the power stage model is put in the left and the control part in the right for a better illustration of the transformation

$$\begin{bmatrix} P' \\ Q' \end{bmatrix} = T \cdot \begin{bmatrix} P \\ Q \end{bmatrix} = \begin{bmatrix} \sin\theta & -\cos\theta \\ \cos\theta & \sin\theta \end{bmatrix} \cdot \begin{bmatrix} P \\ Q \end{bmatrix}. \quad (7)$$

Combining (1), (2), and (7), the virtual active and reactive power flows could be derived following the relationships:

$$P' = \frac{EU_L\phi}{Z} \quad (8)$$

$$Q' = \frac{E\left(E - U_L\right)}{Z}. \quad (9)$$

As a result, the virtual active and reactive power can be uniquely controlled by controlling respectively the frequency and voltage amplitude, which means that power decoupling in the virtual frame is achieved. Fig. 5 presents the decoupled system, which is equivalent to Fig. 4.

However, even though this method could totally decouple the power flows, it cannot guarantee accurate sharing of the actual power, including the active power. When the DGs have different line impedance angles, which is a quite common case, even if the virtual power is perfectly shared, neither the actual active power nor the actual reactive power will be shared [11].

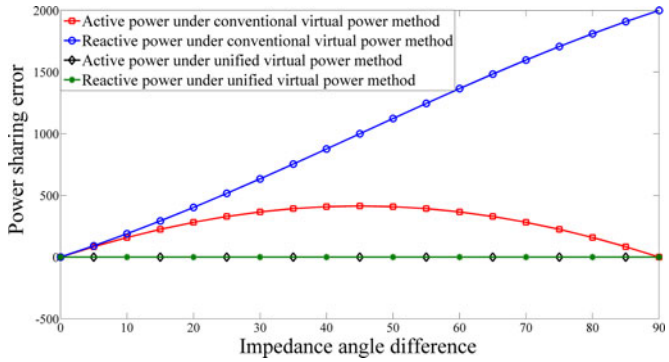


Fig. 6. Power sharing error under different decoupling methods in various cases of line impedance imbalance.

## III. Proposed Control Strategy

### A. Basic Idea

The power sharing problem of the conventional virtual power control is due to the difference of rotation angles. Thus, if the rotation angle is set to be a unified value $\delta$ as expressed in (10), the relationship between the actual power $P$ and $Q$ and the virtual power $\bar{P}$ and $\bar{Q}$ will have nothing to do with the impedance angle of transmission line, and thus will be identical for parallel inverters. Therefore, as long as the virtual power $\bar{P}$ and $\bar{Q}$ are shared, both the actual active power and the actual reactive power will be accurately shared despite the difference of line impedance

$$\begin{bmatrix} \bar{P} \\ \bar{Q} \end{bmatrix} = \bar{T} \cdot \begin{bmatrix} P \\ Q \end{bmatrix} = \begin{bmatrix} \sin\delta & -\cos\delta \\ \cos\delta & \sin\delta \end{bmatrix} \cdot \begin{bmatrix} P \\ Q \end{bmatrix}. \quad (10)$$

Fig. 6 shows the power sharing error under different decoupling methods in various cases of line impedance imbalance of two parallel inverters. For both methods, the virtual power is already equally shared. Nevertheless, it can be seen that the conventional virtual power-based method cannot share the actual power in the case of line impedance imbalance, whereas the proposed method can in any case of line impedance imbalance.

In the unified virtual frame, the virtual power can be shared by controlling independently the frequency and voltage amplitude. The droop relationships are modified as

$$\omega^* = \omega_0 - k_p\left(\bar{P} - \bar{P}_0\right) \quad (11)$$

$$E^* = E_0 - k_q\left(\bar{Q} - \bar{Q}_0\right) \quad (12)$$

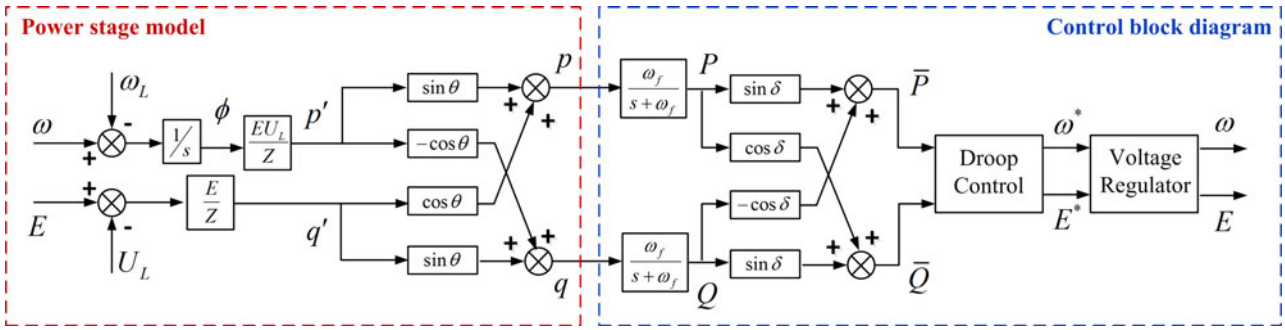


Fig. 7. Block diagram of the virtual power-based decoupling method with a fixed rotation angle.

where $k_p$ and $k_q$ (defined as positive) are the slopes of the $\bar{P}-\omega$ and $\bar{Q}-E$ droop characteristics. The block diagram of the unified virtual power decoupling method with a fixed rotation angle $\delta$ is illustrated in Fig. 7.

Note that in order to share the load power demand among the paralleled DGs, their output virtual power $\bar{P}$ and $\bar{Q}$ have to be shared, which cannot be realized by the decoupling only. Therefore, a proper power sharing strategy is dispensable, which is the limitation of the proposed method compared with the conventional droop control. The accuracy of actual power sharing, including active power, will be affected if the virtual power is poorly shared, whereas the active power is always equally shared under the conventional droop control. Moreover, the active power sharing and the reactive power sharing in this method depend on each other, and it is difficult to share uniquely the active power or the reactive power, while the other kind of power is unshared.

For the simulation and experiments in this paper, in order to achieve a good sharing of virtual power, a $Q-V_{\mathrm{PCC}}$-based indirect voltage control proposed in [20] is selected to be implemented into the unified virtual power-based decoupling method. The power sharing strategy in [20] uses the PCC voltage $V_{\mathrm{PCC}}$ to indirectly control the reactive power $Q$. Differently, in order to combine this power sharing strategy with the proposed decoupling method, the PCC voltage is used here to share the virtual reactive power $\bar{Q}$. In other words, the $Q-V_{\mathrm{PCC}}$ relationship in [20] is modified to be $\bar{Q}-V_{\mathrm{PCC}}$relationship. By adopting the modified power sharing strategy, the effect of line impedance imbalance could be overcome and the virtual reactive power could be shared. As the virtual active power is always shared, the sharing of both actual active and reactive power could be realized.

The following parts of this section are aimed at obtaining the optimal value of the unified rotation angle $\delta$. The optimal angle should be able to guarantee the highest stability. Therefore, the small-signal model of the system is first derived to investigate the system stability.

### B. Small-Signal Modeling of the System Studied

In an LV microgrid, the distribution lines are not typically inductive. The power flows from each DG to the load are expressed as

$$P=\frac{EU_L\phi}{Z}\sin\theta+\frac{E\left(E-U_L\right)}{Z}\cos\theta \tag{13}$$

$$Q=-\frac{EU_L\phi}{Z}\cos\theta+\frac{E\left(E-U_L\right)}{Z}\sin\theta. \tag{14}$$

Combining (13) and (14) with the transformation (10), $\bar{P}$ and $\bar{Q}$ can be expressed as

$$\bar{P}=\frac{EU_L\phi}{Z}\cos\left(\theta-\delta\right)-\frac{E\left(E-U_L\right)}{Z}\sin\left(\theta-\delta\right) \tag{15}$$

$$\bar{Q}=\frac{EU_L\phi}{Z}\sin\left(\theta-\delta\right)+\frac{E\left(E-U_L\right)}{Z}\cos\left(\theta-\delta\right). \tag{16}$$

The small-signal dynamics are obtained by linearizing (15) and (16), and modeling the lower pass filters for power measurement. In addition, further simplification can be done by considering $EU_L/Z >> U_L\phi/Z$. The simplified small-signal model of the unified virtual power is expressed as

$$\Delta\bar{P}=\frac{\omega_f EU_L\cos\left(\theta-\delta\right)}{Z\left(s+\omega_f\right)}\cdot\Delta\phi-\frac{\omega_f\left(2E-U_L\right)\sin\left(\theta-\delta\right)}{Z\left(s+\omega_f\right)}\cdot\Delta E \tag{17}$$

$$\Delta\bar{Q}=\frac{\omega_f EU_L\sin\left(\theta-\delta\right)}{Z\left(s+\omega_f\right)}\cdot\Delta\phi+\frac{\omega_f\left(2E-U_L\right)\cos\left(\theta-\delta\right)}{Z\left(s+\omega_f\right)}\cdot\Delta E \tag{18}$$

where $\delta$ denotes the small deviation of relevant variable from the equilibrium point.

Furthermore, since the bandwidth of the inner voltage loop is much wider than the outer power sharing loop, the output voltage $E$ and frequency $\omega$ can be regarded tracking their own reference $E^*$ and $\omega^*$ perfectly [22], [23]. Therefore, small-signal dynamics of the droop controller are derived by linearizing (11) and (12) in the condition of $\omega=\omega^*$ and $E=E^*$

$$\Delta\omega=-k_p\cdot\left(\Delta\bar{P}-\Delta\bar{P}_0\right) \tag{19}$$

$$\Delta E=-k_q\cdot\left(\Delta\bar{Q}-\Delta\bar{Q}_0\right) \tag{20}$$

and obviously, the phase angle is the integration of the radian frequency

$$\Delta\phi=\frac{\Delta\omega}{s}. \tag{21}$$

Combining (17)–(21), the small-signal model can be eventually described as (22) and (23). The block diagram of the

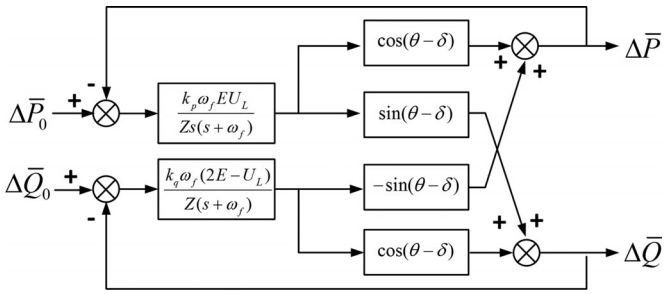


Fig. 8. Block diagrams of the small-signal model of the system.

small-signal model is illustrated in Fig. 8

$$\Delta\bar{P} = \frac{k_p\omega_f EU_L\left(\Delta\bar{P}_0-\Delta\bar{P}\right)}{Zs\left(s+\omega_f\right)}\cdot\cos\left(\theta-\delta\right) - \frac{k_q\omega_f\left(2E-U_L\right)\left(\Delta\bar{Q}_0-\Delta\bar{Q}\right)}{Z\left(s+\omega_f\right)}\cdot\sin\left(\theta-\delta\right) \tag{22}$$

$$\Delta\bar{Q} = \frac{k_p\omega_f EU_L\left(\Delta\bar{P}_0-\Delta\bar{P}\right)}{Zs\left(s+\omega_f\right)}\cdot\sin\left(\theta-\delta\right) + \frac{k_q\omega_f\left(2E-U_L\right)\left(\Delta\bar{Q}_0-\Delta\bar{Q}\right)}{Z\left(s+\omega_f\right)}\cdot\cos\left(\theta-\delta\right). \tag{23}$$

### *C. Optimization of Unified Rotation Angle Based on Stability Investigation*

A standard coupled system with two inputs and two outputs is analyzed in the appendix, based on which the common characteristic polynomial $C$ of the studied system in Fig. 8 can be derived

$$C\left(s\right) = \frac{1}{s(s+\omega_f)^2}\cdot\left[s^3+\left(BY+2\omega_f\right)s^2 + \left(AY+\omega_f\mathrm{BY}+\omega_f^2\right)s+\omega_f AY+AB\right] \tag{24}$$

where

$$A = \frac{k_p\omega_f EU_L}{Z} \tag{25}$$

$$B = \frac{k_q\omega_f(2E-U_L)}{Z} \tag{26}$$

$$Y = \cos\left(\theta-\delta\right). \tag{27}$$

Routh Stability Criterion [24] is applied to investigate the relative stability of the system with different rotation angles. Let $z=s-\sigma$, where $\sigma$ represents the offset between the imaginary axis of the original $s$ frame and that of the newly defined $z$ frame. The Routh array based on the characteristic equation $C\left(z\right)=0$ is shown in Table I, where

$$G_0\left(\sigma,\theta,\delta\right) = -\sigma^3+\sigma^2\left(BY+2\omega_f\right) -\sigma\left(\omega_f BY+AY+\omega_f^2\right)+\omega_f AY+AB \tag{28}$$

TABLE I
ROUTH ARRAY

| | | |
|---|---|---|
| $z^3$ | 1 | $G_1$ |
| $z^2$ | $G_2$ | $G_0$ |
| $z^1$ | $(G_1G_2-G_0)/G_2$ | |
| $z^0$ | $G_0$ | |

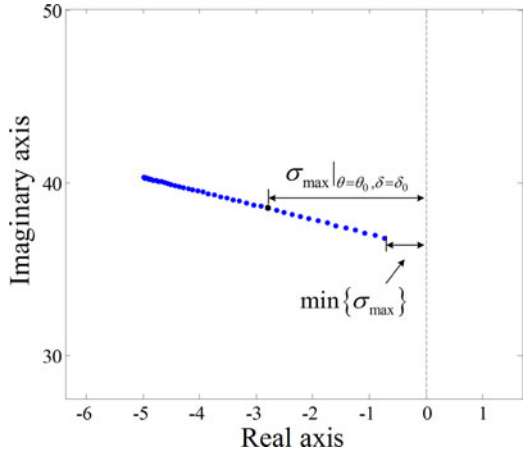


Fig. 9. Variation of $\sigma_{\max}$ with impedance angle $\theta$ changed from 90° to 0° for a given rotation angle $\delta$.

$$G_1\left(\sigma,\theta,\delta\right) = 3\sigma^2-2\sigma\left(2\omega_f+BY\right)+\omega_f BY+AY+\omega_f^2 \tag{29}$$

$$G_2\left(\sigma,\theta,\delta\right) = -3\sigma+BY+2\omega_f. \tag{30}$$

According to Routh Stability Criterion, the system is stable if and only if all terms in the first column of the constructed Routh array are positive. In addition, a larger $\sigma$ indicates a higher relative stability.

Therefore, the problem can be regarded as a problem of nonlinear programming, whose object is to find the maximum value of $\sigma$ within the constrains

$$\begin{cases} G_2>0 \\ \left(G_1G_2-G_0\right)/G_2>0 \\ G_0>0 \\ 0^\circ\le\theta,\delta\le 90^\circ. \end{cases} \tag{31}$$

The maximum value of $\sigma$ varies with the unified rotation angle $\delta$ and the impedance angle $\theta$. As illustrated in Fig. 9, for a given rotation angle $\delta$, the $\sigma_{\max}$, which is the distance from a certain point along the locus to the imaginary axis, will be varied with the impedance angle $\theta$ changed from 90° to 0°. The shortest distance indicates the stability margin of the system under the given rotation angle $\delta$.

If the rotation angle $\delta$ is also changed, the characteristic of $\sigma_{\max}-\delta$ is shown in Fig. 10. The solid lines stand for different impedance angles, while the bold dashed line is the locus via all the lowest points of $\sigma_{\max}$ for each $\delta$. From Fig. 10, we can see that when $\delta$ is set to be 45°, the minimum value of $\sigma_{\max}$ reaches its peak value, which means that the system has the

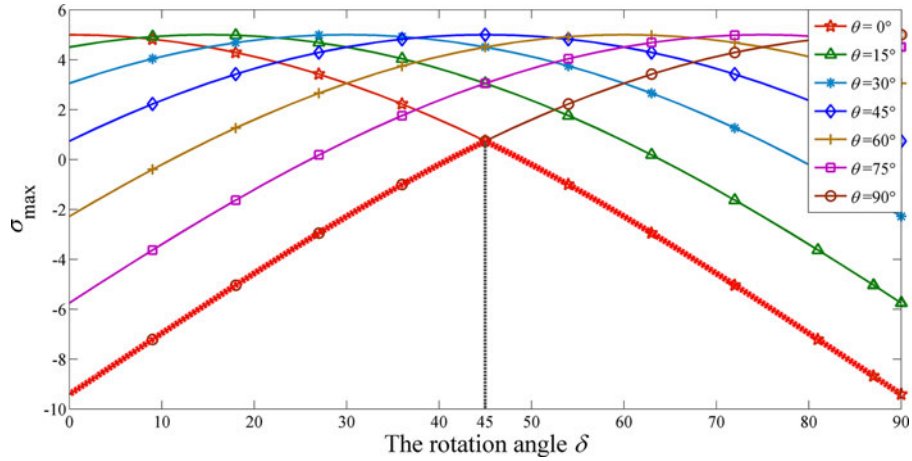


Fig. 10. Characteristic of $\sigma_{\max} - \delta$ where the rotation angle $\delta$ is changed from 0° to 90°.

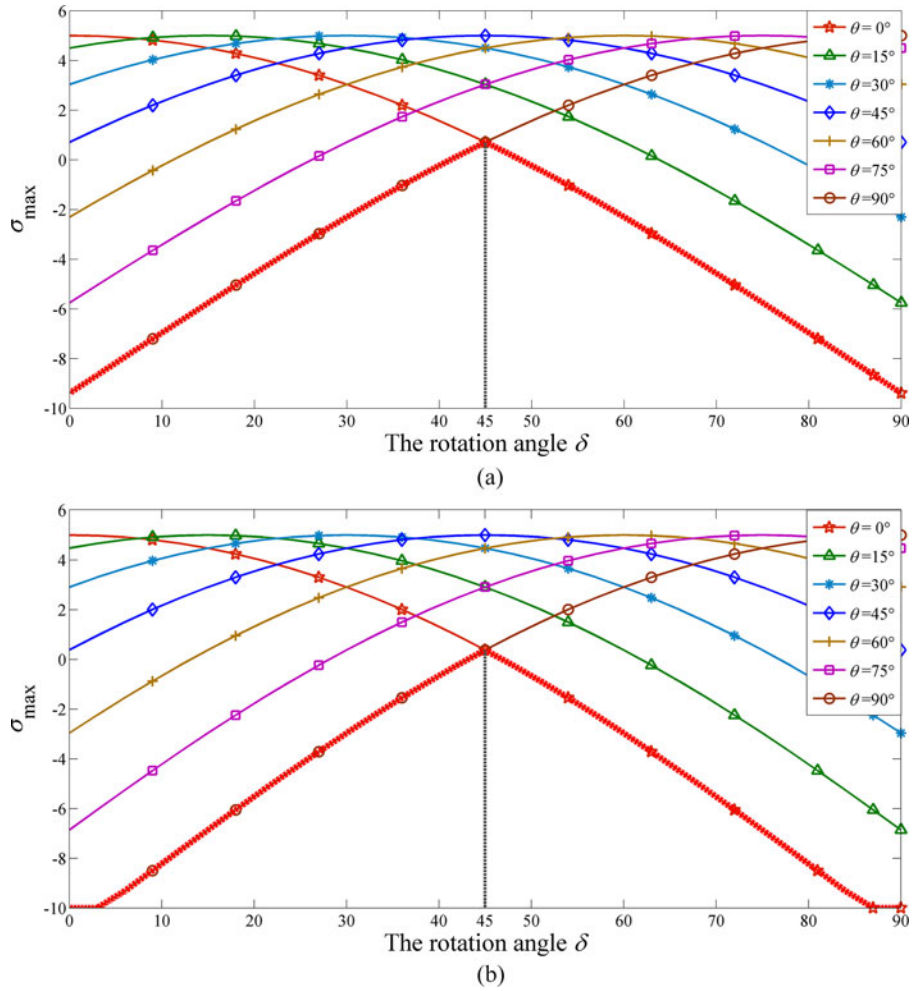


Fig. 11. Characteristics of $\sigma_{\max} - \delta$ with altered parameters. (a) $U_L$ is lowered by 5%. (b) $k_p$ is increased by 50%.

largest stability margin, and thus, it is relatively the most stable when the rotation angel is 45°.

Note that other parameters of the power stage or control variables will also influence the shape of the characteristics $\sigma_{\max} - \delta$. Fortunately, the optimal value of the rotation angle remains the same. Fig. 11 displays two characteristics with altered parameters as examples. Fig. 11(a) is drawn after lowering $U_L$ by 5%. Nevertheless, the curves' shape turns out to be almost the same with that in Fig. 10. Fig. 11(b) is drawn after increasing $k_p$ by 50%. It can be foundthat although the bold

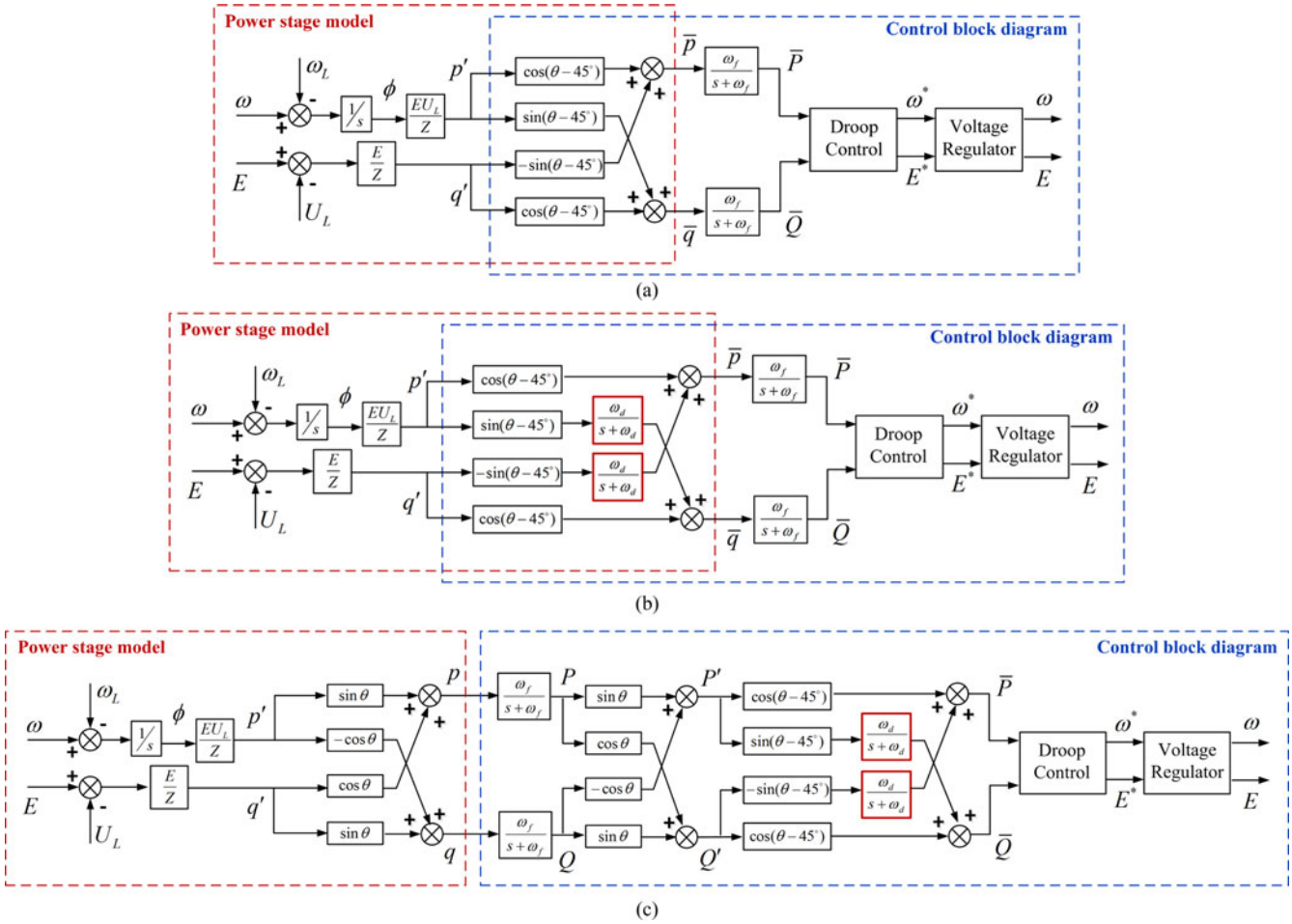


Fig. 12. Block diagrams for introducing decoupling LPFs. (a) Equivalent diagram of the unified virtual power decoupling method. (b) Unified virtual power decoupling with decoupling LPFs. (c) Equivalent diagram of the unified virtual power decoupling method with decoupling LPFs.

dashed curve in Fig. 11(b) is lowered compared with Fig. 10, the optimal rotation angle is still 45°. Therefore, the optimal rotation angle is always 45° despite the change of parameters.

Based on the determined rotation angle, the unified virtual power-based decoupling method is preliminarily established. The unified rotation angle can provide the highest system stability and achieve accurate power sharing in any case of line impedance imbalance as long as the virtual power is equally shared.

## IV. Further Improvement With Decoupling LPFs

The control block diagram of the unified virtual power-based decoupling method shown in Fig. 6, where $\delta = 45°$, can be transformed equivalently into Fig. 12(a). It can be seen from the equivalent control diagram that when $\theta$ changes in the range 0–$\pi$/2, the coefficient (absolute value) of the coupling path, sin($\theta$–45°), is always no larger than that of the noncoupling path, cos($\theta$–45°). Such an observation shows that in this control scheme, the coupling effect is always feebler than the decoupling effect.

In order to further decouple the power control and to guarantee better system stability, LPFs, which serve as a barricade to block the coupling path within the control loop, can be introduced in the coupling paths as shown in Fig. 12(b). With the LPFs, the high-frequency disturbance from the coupling part can hardly affect the relevant control variable, while the low-frequency signals are remained to maintain the steady-state operating point in order to preserve the power sharing ability. Through this way, the control relationships become cleaner and simpler.

In Fig. 12(b), the power stage part and the control part are partly overlapped, which makes it a little turbid for the implementation of the decoupling LPFs. In order to separate the power stage model and the control block diagram, Fig. 12(b) can be equivalently redrawn as (c), from where it can be seen that for the purpose of implementing the decoupling LPFs, the conventional virtual power $P'$ and $Q'$ are still necessary to be employed.

Note that the cutoff radian frequency of the LPFs $\omega_d$ could influence the stability of the system. It needs to be designed with care, which will be discussed in Section V-B.

## V. Stability Analysis and Parameter Design

### A. Stability Analysis of the Proposed Method

In order to investigate the impact of the added LPFs on the system stability, the small-signal model of the system is derived, which is similar to the derivation process shown in Section III-B.

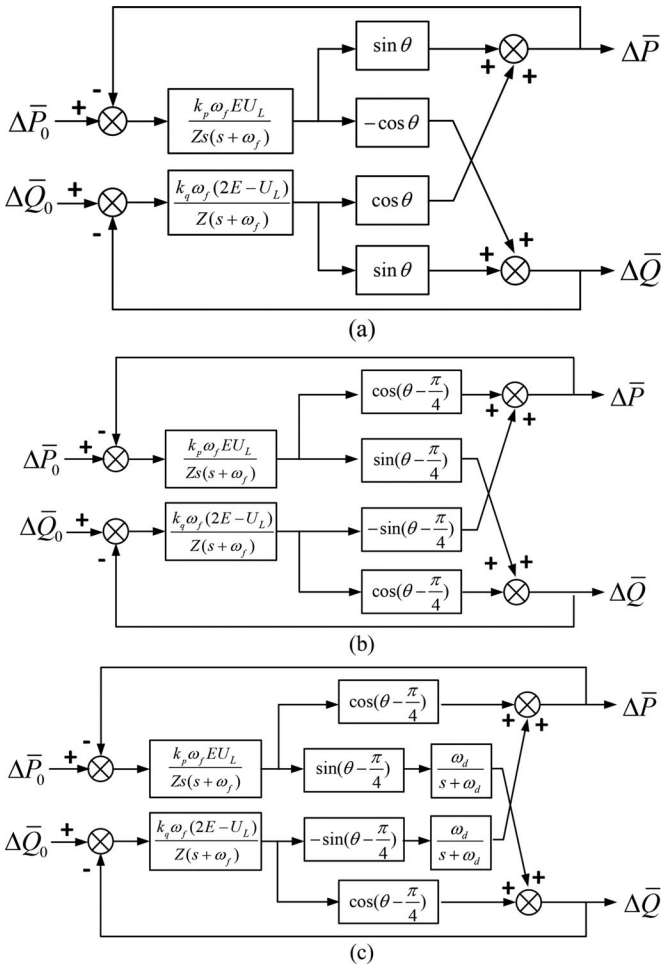


Fig. 13. Block diagrams of small-signal models of different systems. (a) Conventional droop method in the case of inductive–resistive distribution lines. (b) Unified virtual power decoupling method. (c) Unified virtual power decoupling method with decoupling LPFs.

Fig. 13 illustrates the block diagrams of small-signal models of the systems on study, based on which the root loci of the systems can be plotted to show the evolution of root positions with the change of line impedance angle.

Fig. 14(a) shows the root locus of system adopting the conventional droop method. It can be seen that the pair of conjugate poles $\lambda_1$ and $\lambda_2$ move toward the right-half plain as line impedance angle becomes smaller, which means that the system becomes unstable as the resistive component becomes dominant along the distribution line. Fig. 14(b) gives the root locus of system adopting the unified virtual power decoupling method. All roots stay in the left-half plain despite the change of the impedance angle, which indicates that the system is always stable even though the distribution line has large resistive part. Fig. 14(c) shows the root locus of system adopting the LPFs-equipped unified virtual power method. It can be seen from the root locus that compared with Fig. 14(b), an extra pair of conjugate poles $\lambda_4$ and $\lambda_5$ is introduced due to the addition of LPFs. The rightmost position of $\lambda_4$ and $\lambda_5$ are both at the left-half plain. Therefore, $\lambda_4$ and $\lambda_5$ will not affect the system stability substantially since they will never move into the right-half

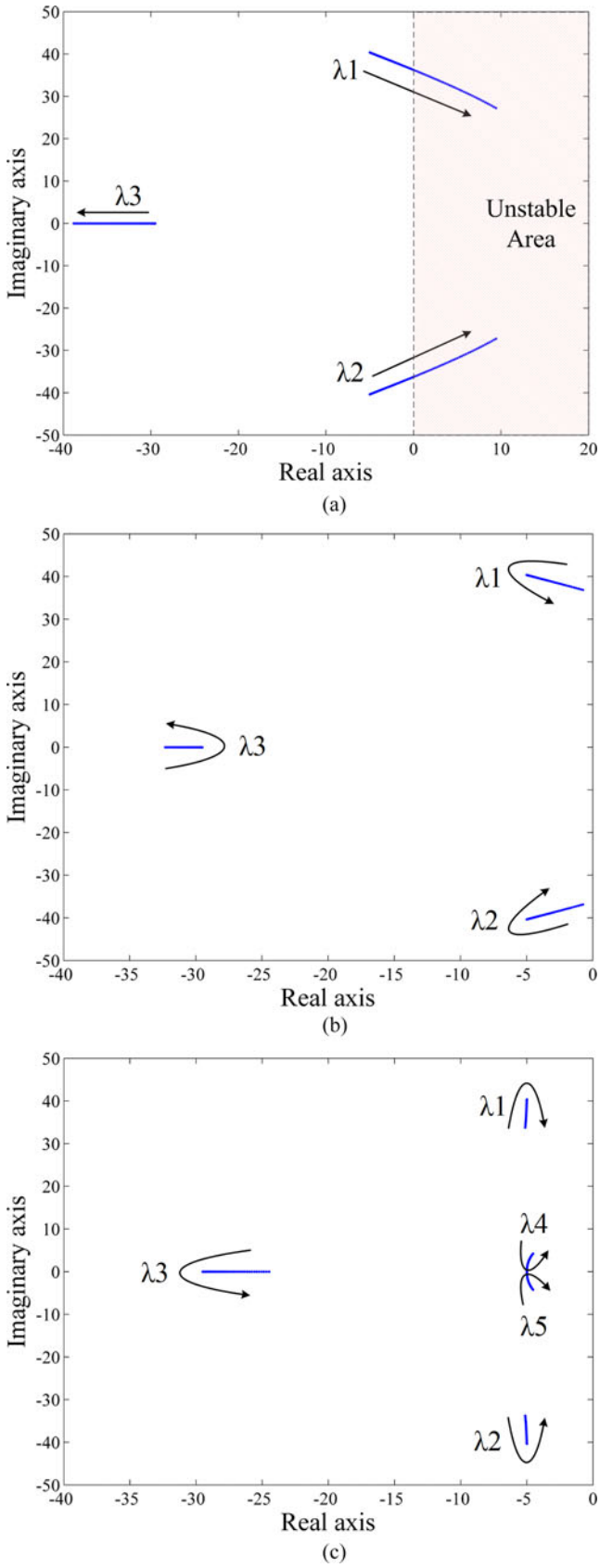


Fig. 14. Root loci of system as line impedance angle decreasing from 90° to 0° with (a) conventional droop method, (b) unified virtual power decoupling method without decoupling LPFs and (c) unified virtual power decoupling method with decoupling LPFs.

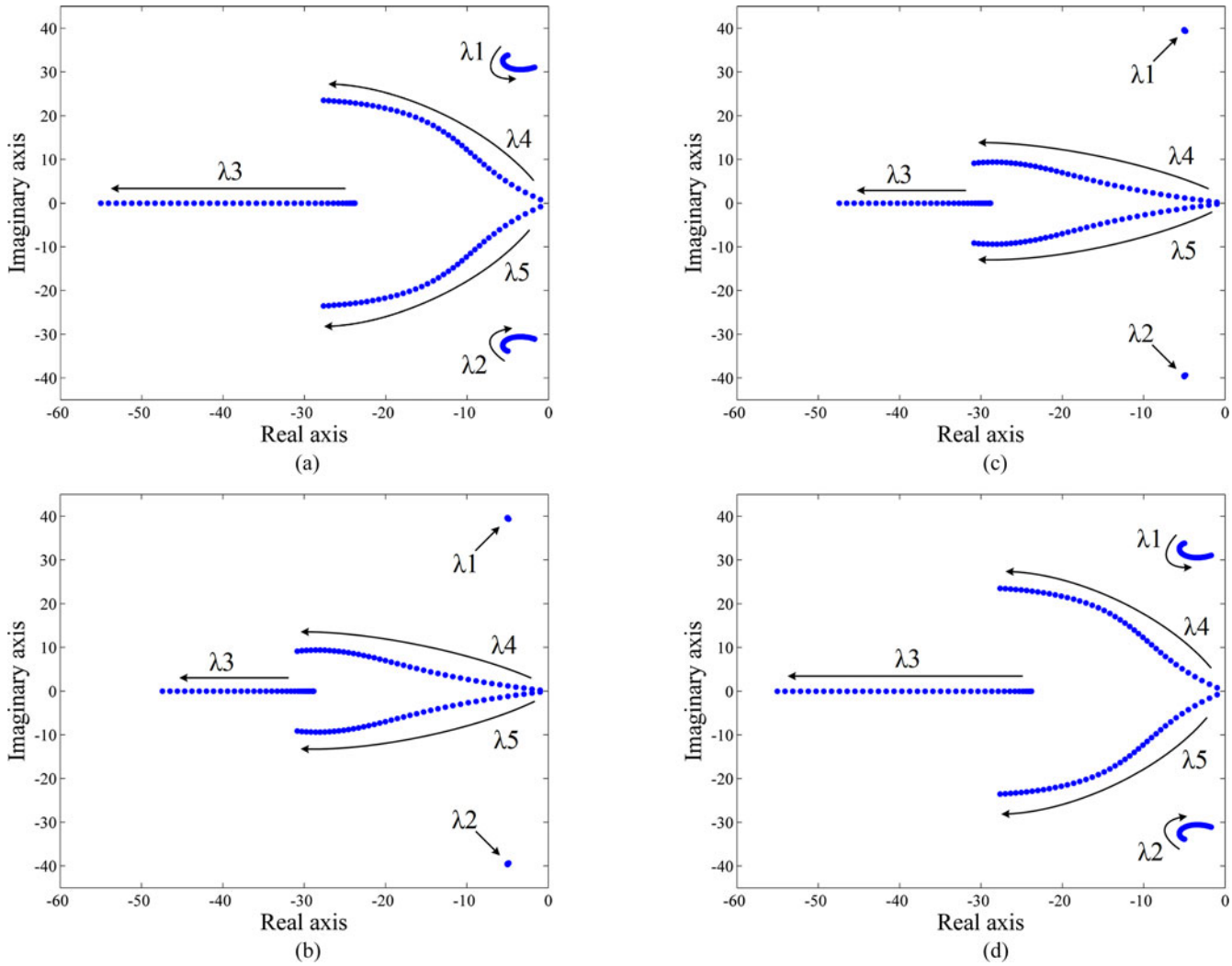


Fig. 15. Root loci of different systems as $\omega_d$ increasing from 0 to 40 rad/s. (a) $\theta = 0°$. (b) $\theta = 30°$. (c) $\theta = 60°$. (d) $\theta = 90°$.

plain. Moreover, in contrast with the conjugate poles $\lambda_1$ and $\lambda_2$ in Fig. 14(b), those in (c) move more slightly, which indicates that the stability of the system with the LPFs is less sensitive to the line impedance angle.

### *B. Design of the Proposed LPFs Considering System Stability*

As the cutoff frequency of the LPFs blocking the coupling paths, $\omega_d$ is a critical parameter requiring careful design for the decoupling of the system. Enlarging or lessening $\omega_d$ too much will both affect the system stability. LPFs with larger $\omega_d$ are less capable at blocking efficiently the high-frequency disturbance via the coupling paths, which will deteriorate the stability. However, LPFs with smaller $\omega_d$ will introduce longer time delays into the power sharing loop, which is also harmful for the stability.

In order to investigate the evolution of system stability with the change of $\omega_d$, the root loci of the system with $\omega_d$ changing from 0 to 40 rad/s are drawn in Fig. 15. It can be seen that after $\omega_d$ reaching to a threshold value (around 16 rad/s), the conjugate poles $\lambda_1$ and $\lambda_2$ begin to move toward the right-hand side with the increasing of $\omega_d$, which indicates that the system stability will be worsened if $\omega_d$ is designed too large, especially in the case that the line impedance angle is near 0° or 90°. On the other hand, if $\omega_d$ is designed too small, the poles $\lambda_4$ and $\lambda_5$ will stay quite close to the right-half plain, which is also bad for the system stability.

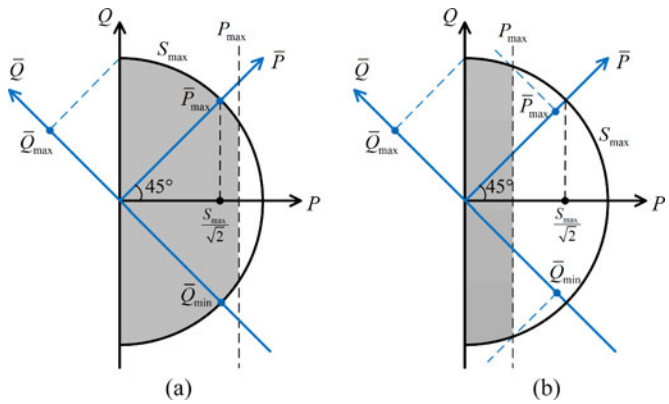


Fig. 16. Operation range of DG in the unified virtual frame. (a) $P_{\max}$ is larger than $S_{\max}/\sqrt{2}$. (b) $P_{\max}$ is not larger than $S_{\max}/\sqrt{2}$.

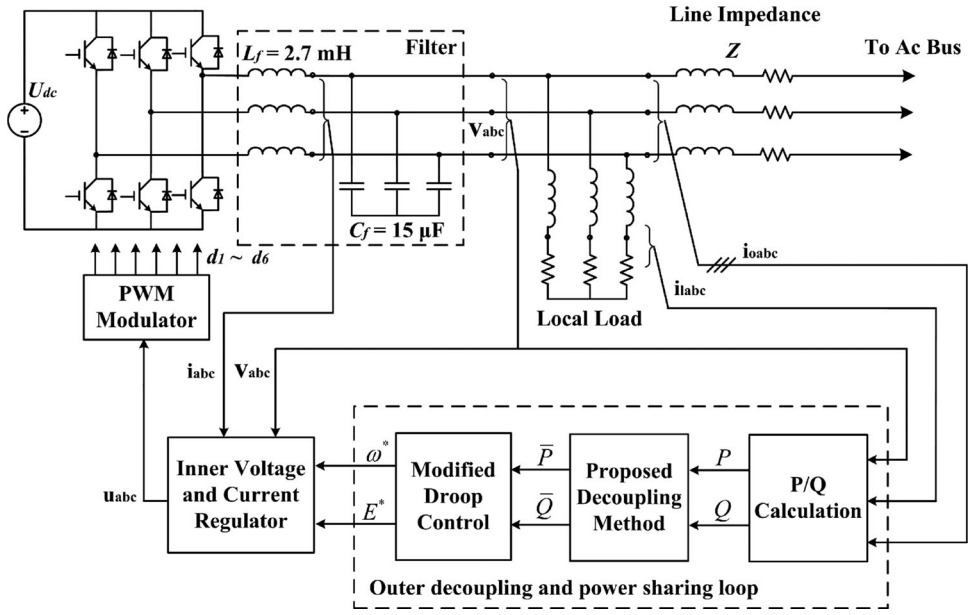


Fig. 17. Structure of the inverter in the microgrid studied.

TABLE II
CONTROL PARAMETERS FOR SIMULATION

| Parameters | Value | Unit |
|---|---|---|
| $P_0$ | 0.0 | kW |
| $Q_0$ | 3.0 | kVar |
| $k_p$ | $1.5 \times 10^{-4}$ | rad/s/W |
| $k_q$ | $5 \times 10^{-3}$ | V/Var |
| $\omega_f$ | 10 | rad/s |
| $\omega_d$ | 5 | rad/s |
| $\omega_0$ | $100\pi$ | rad/s |
| $E_0$ | 310 | V |

As a result, a compromise must be taken into consideration in the design of $\omega_d$. In the simulations and experiments presented in this paper, $\omega_d$ is set at 10 rad/s, which is half of the cutoff frequency $\omega_f$ of the power measurement filters.

### C. Droop Slope Design

The operation range of an inverter is determined by both the maximum active power rating $P_{\max}$ and the maximum apparent power rating $S_{\max}$.$P_{\max}$ is related to the DG prime mover, while $S_{\max}$ is related to the current rating limits [11]. When designing droop slopes for parallel inverters, in order to ensure the inverter operating within the allowed operation range, the power rating and the maximum allowed frequency and voltage deviation should be taken into consideration. The droop slopes in the unified virtual frame are designed by using

$$k_p = \frac{\omega_{\max} - \omega_{\min}}{\bar{P}_{\max}} \tag{32}$$

$$k_q = \frac{E_{\max} - E_{\min}}{\bar{Q}_{\max} - \bar{Q}_{\min}} \tag{33}$$

where $\omega_{\max}$ and $\omega_{\min}$ are the maximum and minimum allowable system frequency. $E_{\max}$ and $E_{\min}$ are the maximum and minimum allowable voltage amplitude. $\bar{P}_{\max}$ is the maximum output virtual active power of the DG. $\bar{Q}_{\max}$ and $\bar{Q}_{\min}$ are respectively the maximum and minimum output virtual reactive power of the DG. The determination of $\bar{P}_{\max}$ and $\bar{Q}_{\min}$ is different in two different cases divided by the relationship between $P_{\max}$ and $\sqrt{2}/2 \cdot S_{\max}$, as illustrated in Fig. 16, where the shaded areas indicate the operation range of the DG.

In the case that $P_{\max}$ is larger than $\sqrt{2}/2 \cdot S_{\max}$, it can be seen from Fig. 16(a) that

$$\bar{P}_{\max} = S_{\max} \tag{34}$$

$$\bar{Q}_{\max} = \frac{\sqrt{2}}{2} S_{\max} \tag{35}$$

$$\bar{Q}_{\min} = -S_{\max}. \tag{36}$$

Differently, in the case that $P_{\max}$ is no larger than $\sqrt{2}/2 \cdot S_{\max}$, it can be seen from Fig. 16(b) that

$$\bar{P}_{\max} = \frac{\sqrt{S_{\max}^2 - P_{\max}^2} + P_{\max}}{\sqrt{2}} \tag{37}$$

$$\bar{Q}_{\max} = \frac{\sqrt{2}}{2} S_{\max} \tag{38}$$

$$\bar{Q}_{\min} = -\frac{\sqrt{S_{\max}^2 - P_{\max}^2} + P_{\max}}{\sqrt{2}}. \tag{39}$$

The droop slopes obtained from (32) and (33) are the maximum values. In practice, the droop slopes can be reduced properly to get higher stability. Furthermore, when DGs of different power rating are connected in parallel, the droop slopes have to be adjusted according to the relationships (40) and (41) to make sure that power is shared proportionally to the power rating of DGs [10]

$$k_{p1} S_{\max 1} = k_{p2} S_{\max 2} = \cdots = k_{pN} S_{\max N} \tag{40}$$

$$k_{q1} S_{\max 1} = k_{q2} S_{\max 2} = \cdots = k_{qN} S_{\max N} \tag{41}$$

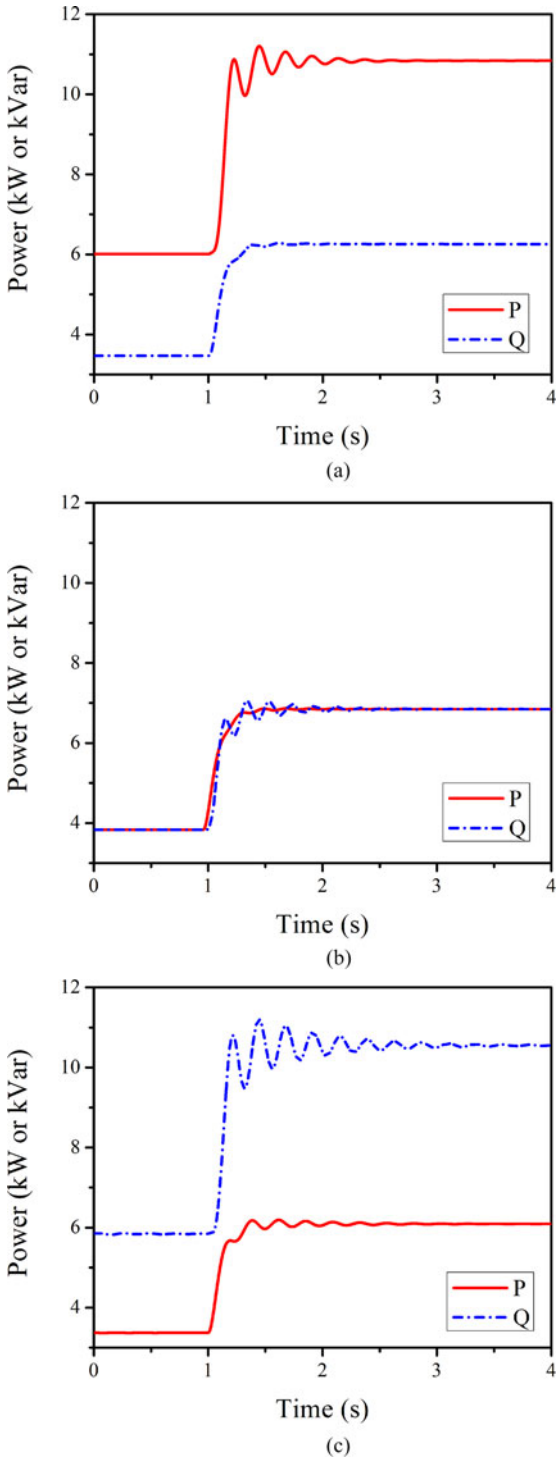


Fig. 18. Power waveforms of systems with different rotation angle $\delta$. (a) $\delta = 30°$. (b) $\delta = 45°$. (c) $\delta = 60°$.

where $k_{pn}$ and $k_{qn}$ ($n = 1, 2, \ldots, N$) are the droop slopes of the $n$th inverter, and $S_{\max n}$ ($n = 1, 2, \ldots, N$) is the maximum apparent power rating of the $n$th inverter.

## VI. Simulation Results

The simulation is conducted with the software PSCAD/EMTDC in various respects. The power stage and the control scheme of one inverter are illustrated in Fig. 17. The control parameters for the simulated inverters are listed in Table II.

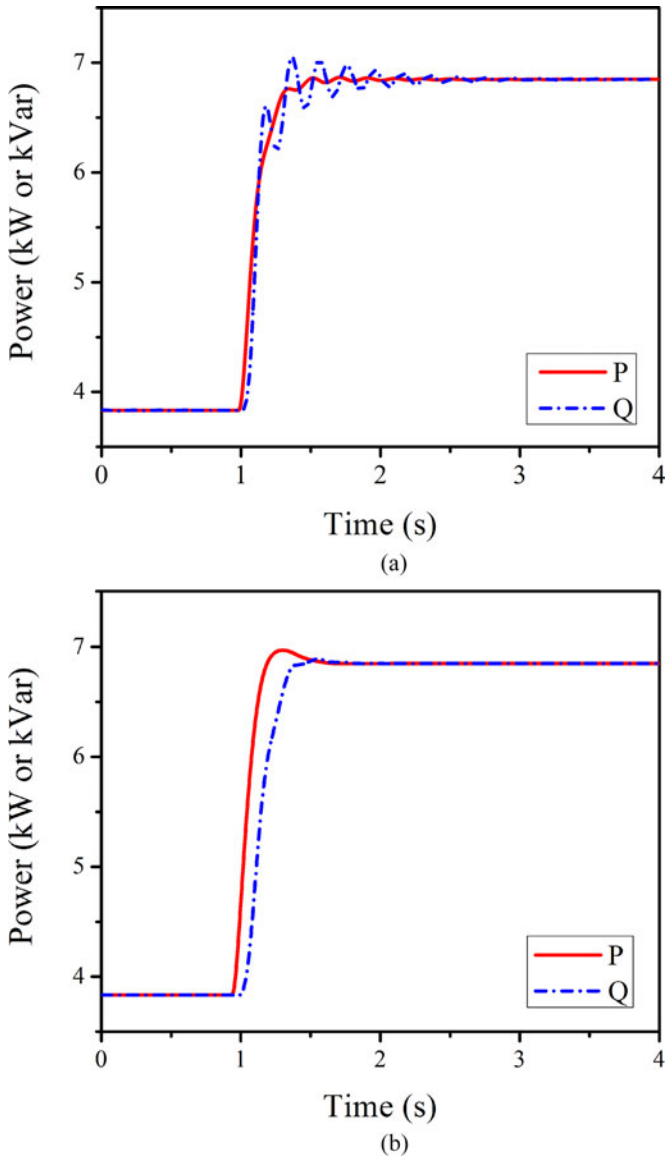


Fig. 19. Power waveforms of system with and without decoupling LPFs. (a) Without decoupling LPFs. (b) With decoupling LPFs.

### A. Verification of the Optimal Rotation Angle

The system configuration for the simulation of this part is shown in Fig. 1. The unified rotation angle $\delta$ is set to be respectively 30°, 45°, and 60° in order to verify through comparison the determination of the optimal rotation angle.

At the end of the first second in the simulation, the PCC voltage drops from 300 to 290 V. Fig. 18 gives the dynamic performance of the system with different rotation angles. The regulating period of the system with a rotation angle of 45° shown in Fig. 18(b) is shorter than that in other cases, which indicates that compared with system (a) and (c), the main roots of system (b) locate farther from the imaginary axis. Therefore,

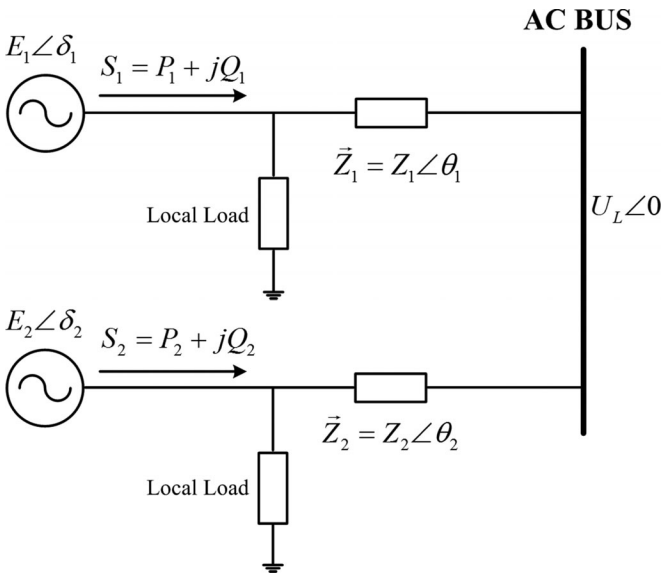


Fig. 20. Two-parallel-inverter system.

TABLE III
DIFFERENT GROUPS OF LINE IMPEDANCE ANGLES

| Inverter No.1 | Inverter No.2 | Angle difference |
|---|---|---|
| 45° | 45° | 0° |
| 60° | 30° | 30° |
| 75° | 15° | 60° |
| 90° | 0° | 90° |

system (b) is relatively more stable. The phenomenon accords well with the analysis in Section III.

### B. Evaluation of the Decoupling LPFs

This part investigates the impact of the decoupling LPFs on the system stability. Fig. 19 shows the dynamic performance of the system when PCC voltage drops from 300 to 290 V at 1 s. The waveforms reveal that the regulating period of system (a) is longer than that of system (b), which indicates that compared with system (a), the main roots of system (b) locate farther from the imaginary axis. Thus, system (b), which is equipped with decoupling LPFs, is relatively more stable. The phenomenon accords well with the analysis in Section V.

### C. Comparison Between Different Decoupling Methods

In this part, a microgrid system with two DGs, as shown in Fig. 20, is employed for the simulation.

In order to illustrate the advantage of the proposed decoupling method, comparison between different control methods is made in this part. Fig. 21(a) shows the comparison between conventional droop method and the proposed decoupling method. At the beginning, both inverters adopt conventional droop control and their line impedances are both 3 mH. At 3 s, the line impedance of inverter No.1 is changed from 3 mH to 1 Ω. Consequently, the system becomes unstable and the power waveforms

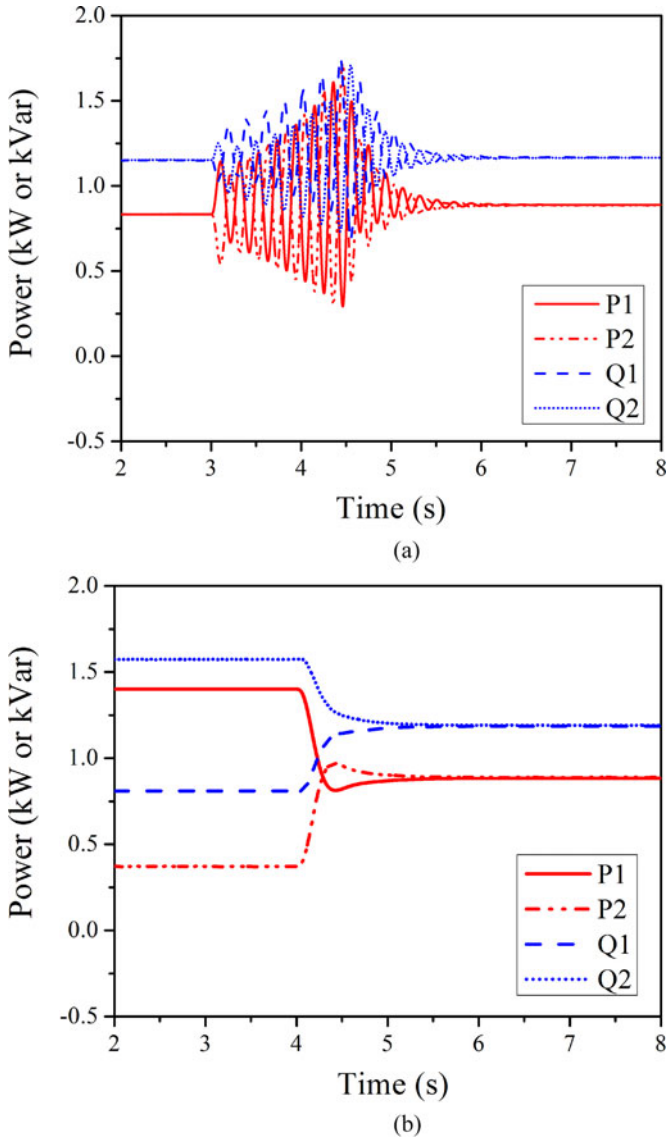


Fig. 21. Comparison between different control methods: (a) Conventional droop method and unified virtual power method, (b) conventional virtual power method and unified virtual power method.

begin to oscillate. The proposed method is activated at 4.5 s and from then on, the system gradually returns to stable.

Fig. 21(b) shows the switching from the conventional virtual power-based method to the proposed method. The line impedance of inverter No.1 is 3 mH + 1 Ω while that of inverter No.2 is 3 mH. Both inverters adopt conventional virtual power-based method before 4 s. It can be found that neither the active nor the reactive power is shared. The proposed method is activated at 4 s, and consequently, both the active and the reactive power are shared accurately.

### D. Proposed Decoupling Method With Various Impedance Situations

This part investigates the power sharing performance of the system with various impedance angle differences between parallel inverters. The system simulated is still as Fig. 20. The various

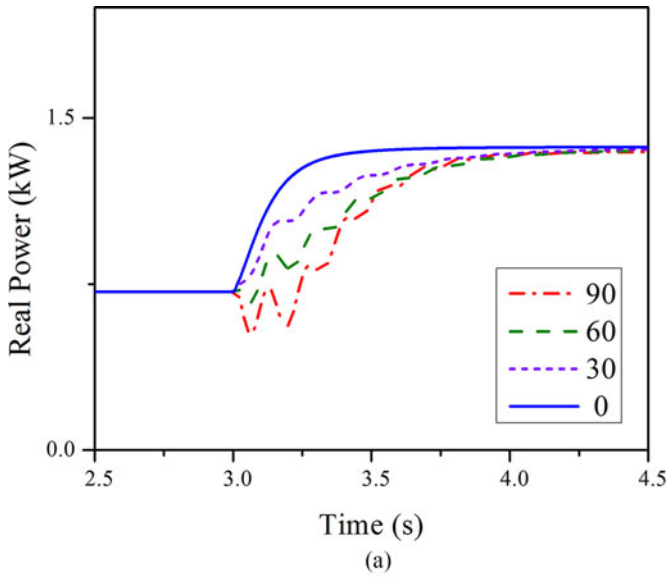


Fig. 22. Performance of the proposed decoupling method in different cases of line impedance. (a) Waveforms of the active power. (b) Waveforms of the reactive power.

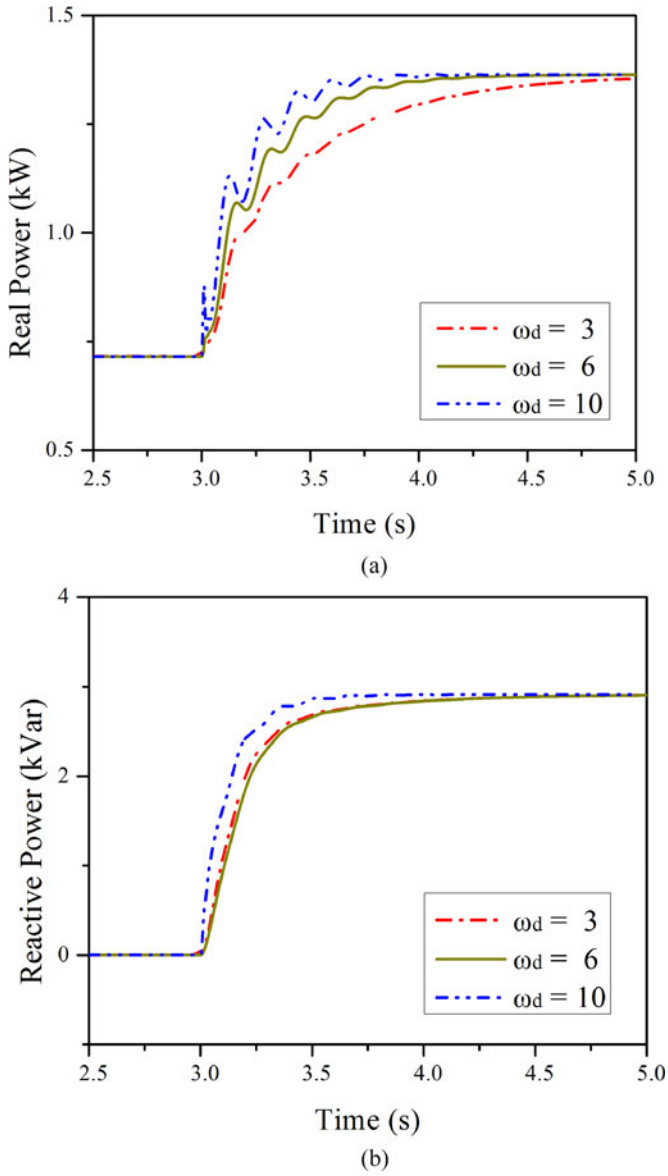


Fig. 23. Performance of the proposed decoupling method in case of different $\omega_d$ (in unit of rad/s). (a) Waveforms of the active power. (b) Waveforms of the reactive power.

impedance angles are listed in Table III. Fig. 22 shows the dynamic response of both the active and the reactive power output by inverter No.1. It can be seen that when the impedance angles of the two inverters differ largely, the dynamic response becomes slower and fluctuates more severely. However, the system can always get stable and share power accurately. In other words, the proposed method is highly adaptable to various line impedance situations.

### *E. Proposed Decoupling Method With Different $\omega_d$*

This part illustrates by simulation the tradeoff in the design of $\omega_d$. The system configuration is the same with the previous part. Various $\omega_d$ are adopted in this part to investigate the impact of the decoupling LPFs on the dynamic performance of the system. Fig. 23 shows the dynamic response of the output power of the proposed method. It can be seen that smaller $\omega_d$ leads to a longer rising time due to the time delay brought on by the LPFs, while larger $\omega_d$ results in more severe oscillations since the LPFs in this case function feebly, and thus, the decoupling effect is weaker. This well verifies the discussion in Section V-B.

## VII. Laboratory Test Results

The proposed decoupling strategy is verified in this section with laboratory setups, configured as Fig. 20, which consists of two paralleled three-phase inverters (MWINV-9R144) controlled by a 32-bit floating-point 150 MHz digital signal processor TMS320F28335 from Texas Instruments. The power stage and the control scheme of each inverter are illustrated in Fig. 17. The essential parameters are listed in Table IV, where the symbol $\rightarrow$ indicates the changing of the corresponding parameter

TABLE IV
PARAMETERS FOR EXPERIMENTS

| Parameters | Value | Unit |
|---|---|---|
| $P_0$ | 2.0 | kW |
| $Q_0$ | 3.0 | kVar |
| $k_p$ | $1.5 \times 10^{-4}$ | rad/s/W |
| $k_q$ | $5 \times 10^{-3}$ | V/Var |
| $\omega_f$ | 10 | rad/s |
| $\omega_d$ | 5 | rad/s |
| $\omega_0$ | $100\pi$ | rad/s |
| $E_0$ | $200\sqrt{2}$ | V |
| $Z_1$ | $j0.94$ | Ω |
| $Z_2$ in Part A | $2 + j0.94 \rightarrow 2$ | Ω |
| $Z_2$ in Part B | 2 | Ω |

from one value to another. The voltage and current waveforms are acquired by directly printing the screen of HIOKI Power Analyzer 3390, while the active and the reactive power waveforms are drawn in OriginPro based on the recorded data of the Power Analyzer 3390.

### A. Power Decoupling Effect

This part validates by experiments the power decoupling effect of the proposed method, and Fig. 24 shows the waveforms of the active and the reactive power during the whole process. At the beginning, both inverters adopt conventional droop control method, and their line impedances are listed in Table IV.

At the moment $t_1$, the line impedance of inverter No.2 is changed from resistive–inductive to purely resistive as shown in Table IV. The system begins to oscillate since $t_1$ and the voltage and current waveforms of the parallel inverters are presented in Fig. 25(a), where the phase difference between the current of two inverters is changing, which indicates the fluctuation of the output power due to the instability.

At the moment $t_2$, the proposed decoupling method is activated. As a result, the oscillation is attenuated and the system returns to stable, and it can be found in Fig. 25(b) that the phase difference between the output current of parallel inverters becomes invariable.

### B. Power Sharing Performance

This part of experiments aims at investigating the power sharing performance of the proposed control method, and the line impedance of inverter No. 2 is set to be purely resistive as listed in Table IV. Comparison between the proposed method and the conventional virtual power-based method is presented, and the waveforms of the active and the reactive power during the whole process are shown in Fig. 26.

At the beginning, both inverters adopt conventional virtual power-based method. It can be found that neither the active nor reactive power is shared due to the line impedance imbalance. The voltage and current waveforms of the parallel inverters are presented in Fig. 27(a), and it can be seen that the voltage phase difference is different from the current phase difference, which indicates a poor power sharing performance of the conventional virtual power-based method.

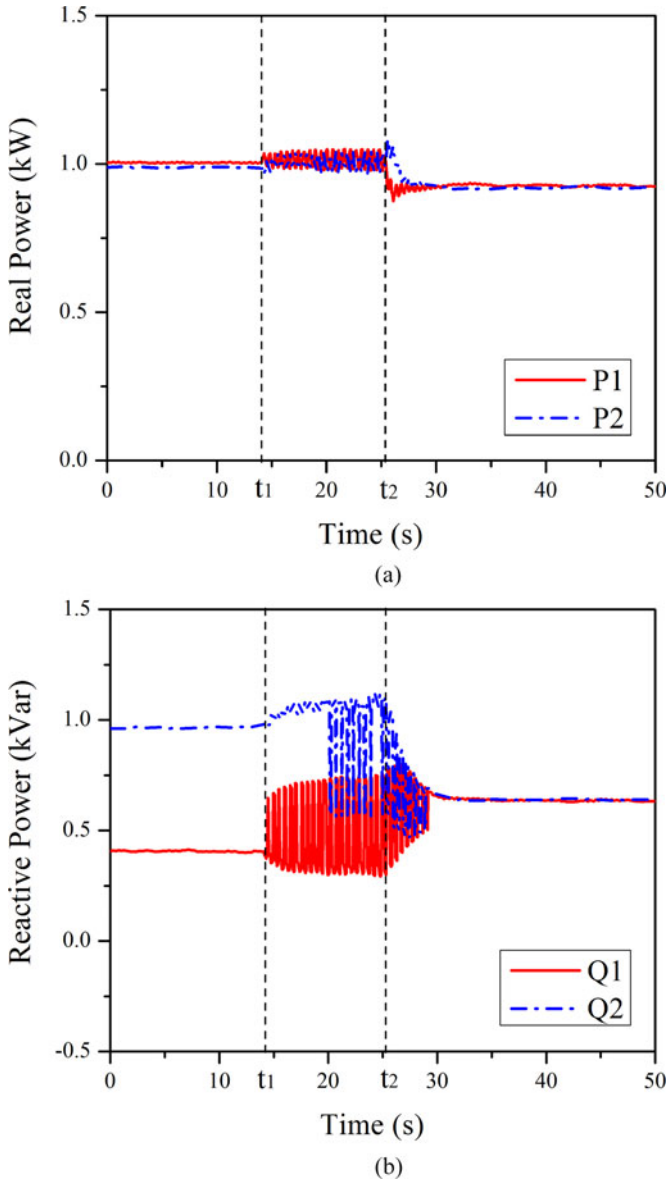


Fig. 24. Test of decoupling effect of the proposed method: (a) Waveforms of the active power, (b) Waveforms of the reactive power.

At the moment $t_1$, the proposed decoupling method is enabled and both the active power and the reactive power become accurately shared since then. It can be seen in Fig. 27(b) that the voltage phase difference is the same as the current phase difference, which signifies a good power sharing performance of the proposed method.

## VIII. CONCLUSION

An improved decoupling method based on the unified virtual power is proposed in this paper to achieve good system stability and accurate power sharing among parallel DGs in microgrids. The influence of the rotation angle on the system stability is mathematically analyzed, based on which the optimal value of the rotation angle is derived. By employing a unified power transformation and implementing LPFs to further block the

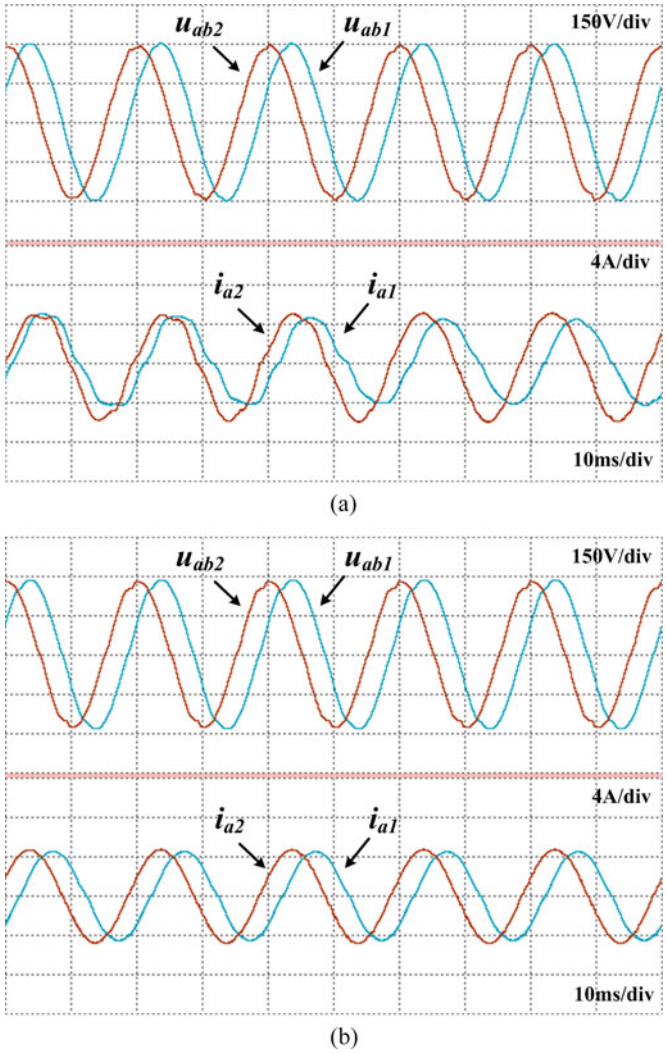


Fig. 25. Voltage and current waveforms of the parallel inverters with (a) conventional droop control and (b) proposed control method.

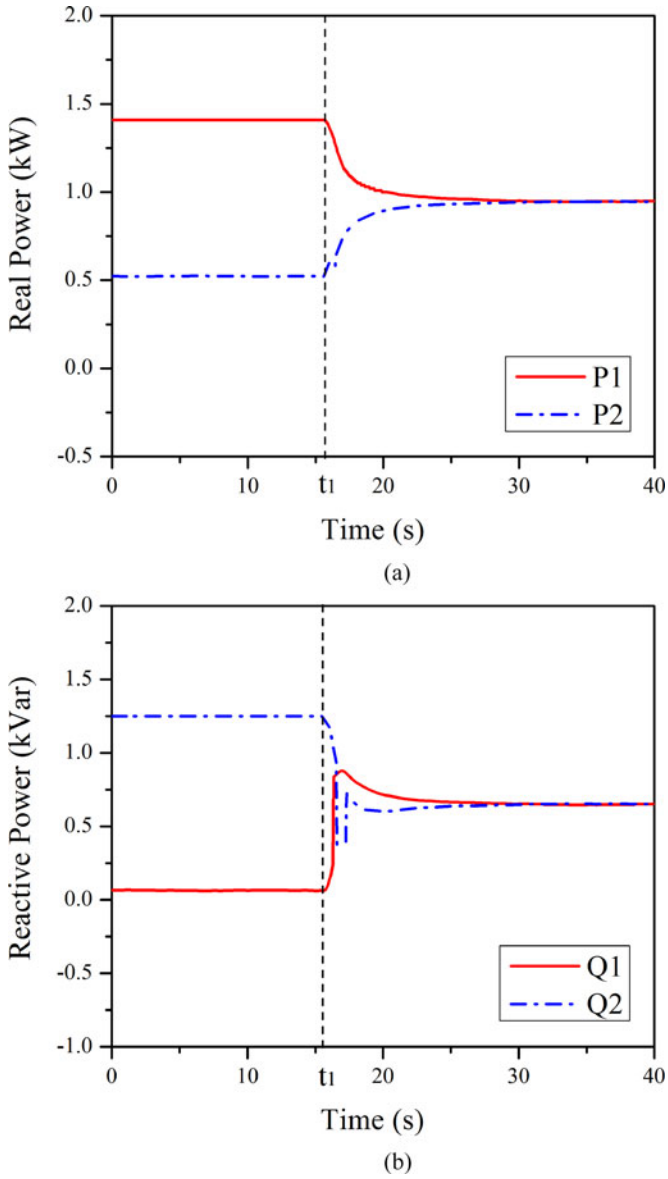


Fig. 26. Test of power sharing effect of the proposed method: (a) Waveforms of the active power, (b) waveforms of the reactive power.

coupling paths, the proposed method can effectively realize power decoupling and, thus, ensure good system stability. Equal power sharing among parallel DGs can also be realized by equally sharing the virtual power. The impact of the proposed method upon the system stability is analyzed in detail. The design of the decoupling LPFs and of the droop slopes is also presented. The effectiveness of the proposed decoupling method is verified by both simulation and experiments.

## APPENDIX

In this section, a more general system with similar structure to the system analyzed in Section III is taken as example. Fig. 28 shows the configuration of the system, where $G_{11}$ and $G_{22}$ are the transfer functions along the noncoupling paths, while $G_{12}$ and $G_{21}$ are that along the coupling paths. $G_{c1}$ and $G_{c2}$ are the transfer functions of the common forward paths.

Based on the block diagram in Fig. 28, the following equations can be easily derived:

$$(u_1 - y_1)\, G_{11}G_{c1} + (u_2 - y_2)\, G_{12}G_{c2} = y_1 \qquad \text{(A.1)}$$

$$(u_1 - y_1)\, G_{21}G_{c1} + (u_2 - y_2)\, G_{22}G_{c2} = y_2. \qquad \text{(A.2)}$$

Equations (A.1) and (A.2) can be transformed as

$$y_1 = \frac{G_{11}G_{c1} + G_{c1}G_{c2}\,(G_{11}G_{22} - G_{12}G_{21})}{C}u_1 + \frac{G_{12}G_{c2}}{C}u_2 \qquad \text{(A.3)}$$

$$y_2 = \frac{G_{22}G_{c2} + G_{c1}G_{c2}\,(G_{11}G_{22} - G_{12}G_{21})}{C}u_2 + \frac{G_{12}G_{c1}}{C}u_1 \qquad \text{(A.4)}$$

$$C = (1+G_{11}G_{c1})\,(1 + G_{22}G_{c2}) - G_{12}G_{21}G_{c1}G_{c2}. \qquad \text{(A.5)}$$

$C$ is the common characteristic polynomial of the coupled system and $C = 0$ is the characteristic equation. According to the automatic control theory, the system is stable if and only if all roots of the characteristic equation have negative real parts,

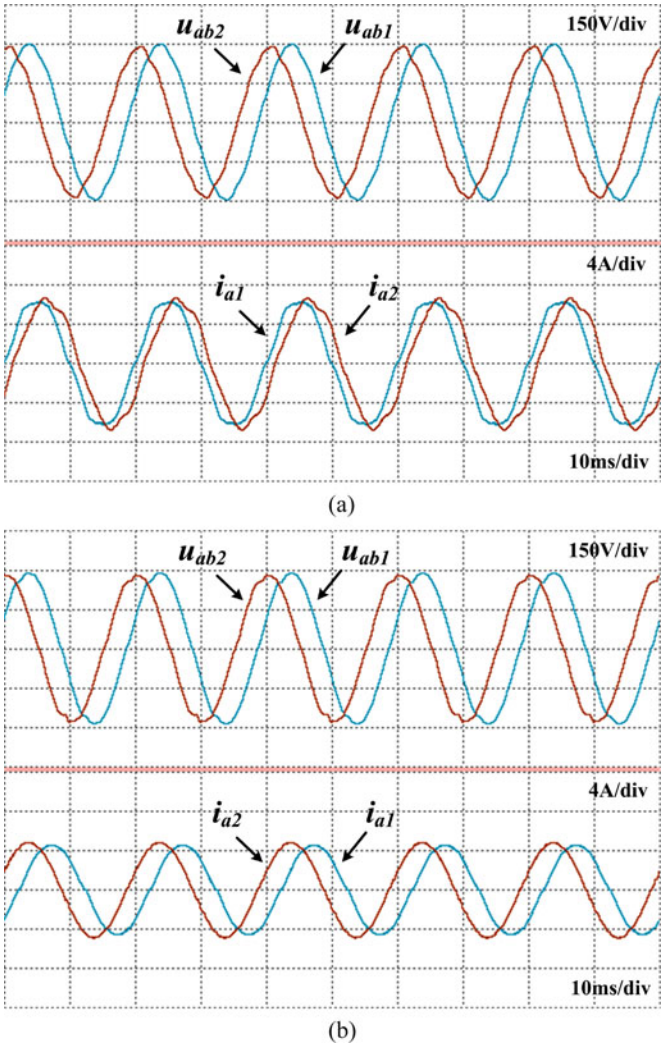


Fig. 27. Voltage and current waveforms of parallel inverters with (a) conventional virtual power based method and (b) proposed control method.

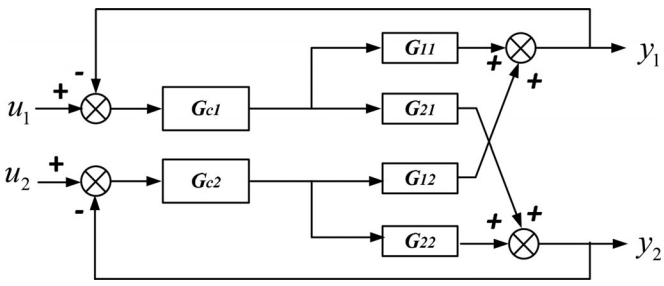


Fig. 28. Block diagram of the coupled system on study.

based on which Routh Stability Criterion can be applied to investigate the system stability in Sections III and V.

## REFERENCES


[1] P. Piagi and R. H. Lasseter, "Autonomous control of microgrids," in *Proc. Power Eng. Soc. Gen. Meet.*, Montreal, QC, Canada, 2006, pp. 1–8.

[2] J. M. Guerrero, M. Chandorkar, T. Lee, and P. C. Loh, "Advanced control architectures for intelligent Microgrids—Part I: Decentralized and hierarchical control," *IEEE Trans. Ind. Electron.*, vol. 60, no. 4, pp. 1254–1262, Apr. 2013.

[3] J. Rocabert, A. Luna, F. Blaabjerg, and P. Rodríguez, "Control of power converters in AC microgrids," *IEEE Trans. Power Electron.*, vol. 27, no. 11, pp. 4734–4749, Nov. 2012.

[4] R. P. S. Chandrasena, F. Shahnia, S. Rajakaruna, and A. Ghosh, "Control, operation and power sharing among parallel converter-interfaced DERs in a microgrid in the presence of unbalanced and harmonic loads," in *Proc. Australas. Univ. Power Eng. Conf.*, Hobart, Tas., Australia, 2013, pp. 1–6.

[5] R. H. Lasseter, "MicroGrids," in *Proc. Power Eng. Soc. Winter Meet.*, 2002, pp. 305–308.

[6] R. H. Lasseter, "Smart distribution: Coupled microgrids," in *Proc. IEEE*, vol. 99, no. 6, pp. 1074–1082, Jun. 2011.

[7] B. Kroposki, C. Pink, R. DeBlasio, H. Thomas, M. Simoes, and P. K. Sen, "Benefits of power electronic interfaces for distributed energy systems," *IEEE Trans. Energy Convers.*, vol. 25, no. 3, pp. 901–908, Sep. 2010.

[8] A. Khalil, K. A. Alfaitori, and A. Elbarsha, "Stability analysis of parallel-inverters in microgrid," in *Proc. Int. Conf. Autom. Comput.*, Cranfield, U.K., 2014, pp. 110–115.

[9] J. M. Guerrero, J. Matas, L. G. De Vicuña, M. Castilla, and J. Miret, "Wireless-control strategy for parallel operation of Distributed-generation inverters," *IEEE Trans. Ind. Electron.*, vol. 53, no. 5, pp. 1461–1470, Oct. 2006.

[10] J. M. Guerrero, L. Hang, and J. Uceda, "Control of distributed uninterruptible power supply systems," *IEEE Trans. Ind. Electron.*, vol. 55, no. 8, pp. 2845–2859, Aug. 2008.

[11] Y. Li and Y. W. Li, "Power management of inverter interfaced autonomous microgrid based on virtual Frequency-voltage frame," *IEEE Trans. Smart Grid*, vol. 2, no. 1, pp. 30–40, Mar. 2011.

[12] J. A. Peas Lopes, C. L. Moreira, and A. G. Madureira, "Defining control strategies for MicroGrids islanded operation," *IEEE Trans. Power Syst.*, vol. 21, no. 2, pp. 916–924, May 2006.

[13] Y. W. Li and C. N. Kao, "An accurate power control strategy for power-electronics-interfaced distributed generation units operating in a low-voltage multibus microgrid," *IEEE Trans. Power Electron.*, vol. 24, no. 12, pp. 2977–2988, Dec. 2009.

[14] J. He and Y. W. Li, "Analysis, design, and implementation of virtual impedance for power electronics interfaced distributed generation," *IEEE Trans. Ind. Appl.*, vol. 47, no. 6, pp. 2525–2538, Nov./Dec. 2011.

[15] J. M. Guerrero, L. G. De Vicuña, J. Matas, M. Castilla, and J. Miret, "Output impedance design of parallel-connected UPS inverters with wireless load-sharing control," *IEEE Trans. Ind. Appl.*, vol. 52, no. 4, pp. 1126–1135, Aug. 2005.

[16] J. He, Y. W. Li, J. M. Guerrero, F. Blaabjerg, and J. C. Vasquez, "An islanding microgrid power sharing approach using enhanced virtual impedance control scheme," *IEEE Trans. Power Electron.*, vol. 28, no. 11, pp. 5272–5282, Nov. 2013.

[17] Y. Zhu, Z. Fang, F. Wang, B. Liu, and Y. Zhao, "A wireless load sharing strategy for islanded microgrid based on feeder current sensing," *IEEE Trans. Power Electron.*, vol. 30, no. 12, pp. 6706–6719, Dec. 2015.

[18] J. He, Y. W. Li, and F. Blaabjerg, "An enhanced islanding microgrid reactive power, imbalance power, and harmonic power sharing scheme," *IEEE Trans. Power Electron.*, vol. 30, no. 6, pp. 3389–3401, Jun. 2015.

[19] K. D. Brabandere, B. Bolsens, J. Van Den Keybus, A. Woyte, J. Driesen, R. Belmans, and K. U. Leuven, "A voltage and frequency droop control method for parallel inverters," *IEEE Trans. Power Electron.*, vol. 22, no. 4, pp. 2501–2507, Jul. 2007.

[20] X. Zhang, J. Liu, Z. You, and T. Liu, "Study on the influence of distribution lines to parallel inverter systems adopting the droop control method," *J. Power Electron.*, vol. 13, no. 4, pp. 701–711, Jul. 2013.

[21] J. M. Guerrero, J. C. Vasquez, J. Matas, M. Castilla, and L. G. De Vicuna, "Control strategy for flexible microgrid based on parallel line-interactive UPS systems," *IEEE Trans. Ind. Electron.*, vol. 56, no. 3, pp. 726–736, Mar. 2009.

[22] E. A. A. Coelho, P. C. Cortizo, and P. F. D. Garcia, "Small-signal stability for parallel-connected inverters in stand-alone AC supply systems," *IEEE Trans. Ind. Appl.*, vol. 38, no. 2, pp. 533–542, Mar./Apr. 2002.

[23] N. Pogaku, M. Prodanovic, and T. C. Green, "Modeling, analysis and testing of autonomous operation of an inverter-based microgrid," *IEEE Trans. Power Electron.*, vol. 22, no. 2, pp. 613–625, Mar. 2007.

[24] R. C. Dorf and R. H. Bishop, *Modern Control Systems*, 11th ed. Englewood Cliffs, NJ, USA: Prentice-Hall, 2008, ch. 6.

[25] W. Yao, M. Chen, J. Matas, M. Guerrero, and Z. Qian, "Design and analysis of the droop control method for parallel inverters considering the impact of the complex impedance on the power sharing," *IEEE Trans. Ind. Electron.*, vol. 58, no. 2, pp. 576–588, Feb. 2011.
[26] H. Mahmood, D. Michaelson, and J. Jiang, "Accurate reactive power sharing in an islanded microgrid using adaptive virtual impedance," *IEEE Trans. Power Electron.*, vol. 30, no. 3, pp. 1605–1617, Mar. 2015.
[27] C. N. Rowe, T. J. Summers, R. E. Betz, D. J. Cornforth, and T. G. Moore, "Arctan power-frequency droop for improved microgrid stability," *IEEE Trans. Power Electron.*, vol. 28, no. 8, pp. 3747–3759, Aug. 2013.

**Teng Wu** (S'15) received the B.S. degree in electrical engineering from Xi'an Jiaotong University, Xi'an, China, in 2012, where he is currently working toward the Ph.D. degree at the School of Electrical Engineering.

His current research interests include renewable energy, mainly focusing on the coordinative control of droop-based paralleled converters in AC microgrid.

**Zeng Liu** (S'09–M'14) received the B.S. degree from Hunan University, Changsha, China, and the M.S. and Ph.D. degrees from Xi'an Jiaotong University (XJTU), Xi'an, China, in 2006, 2009, and 2013, respectively, all in electrical engineering.

He is currently at the Faculty of Electrical Engineering, XJTU. His research interests include control of single-phase and multiphase power converters for uninterrupted power supply and utility application, modeling, analysis, and control of distributed power system based on three-phase AC bus.

**Jinjun Liu** (M'97–SM'10) received the B.S. and Ph.D. degrees in electrical engineering from Xi'an Jiaotong University (XJTU), Xi'an, China, in 1992 and 1997, respectively.

He then joined the XJTU Electrical Engineering School as a Faculty. In 1997, 1999, and 2010, respectively, he participated in technology, professional, and management training programs at the Advanced Technology Laboratories, Inc., Signal Hill, CA, USA, the Milwaukee School of Engineering, Milwaukee, WI, USA, and the Chinese University of Hong Kong, Hong Kong. From late 1999 until early 2002, he was with the Center for Power Electronics Systems, Virginia Polytechnic Institute and State University, Blacksburg, VA, USA, as a Visiting Scholar. In late 2002, he was promoted to a Full Professor and then the Head of the Power Electronics and Renewable Energy Center at XJTU, which now comprises 14 faculty members and 120 graduate students and carries one of the leading power electronics programs in China. He served as an Associate Dean of Electrical Engineering School at XJTU from 2005 to early 2010, and the Dean for the Undergraduate Education of XJTU from 2009 to early 2015. He currently holds the position of XJTU Distinguished Professor of Power Electronics, sponsored by Chang Jiang Scholars Program of Chinese Ministry of Education. He coauthored 3 books, published more than 200 technical papers in peer-reviewed journals and conference proceedings, holds 25 patents. His research interests include power quality control and utility applications of power electronics, and microgrids for sustainable energy and distributed generation.

Dr. Liu received several governmental awards at national level or provincial level for scientific or career achievements and the 2006 Delta Scholar Award. He has served as the IEEE Power Electronics Society (PELS) Region 10 Liaison and then China Liaison for eight years, an Associate Editor for the IEEE TRANSACTIONS ON POWER ELECTRONICS for eight years, and starting from 2015 the Executive Vice President membership for PELS. He chaired the Asian Power Electronics Conferences Coordinating Committee from June 2012 to May 2014. He is on Board of China Electrotechnical Society (CES) and was elected to the Vice President of the CES Power Electronics Society in 2013. He is also on the Executive Board and was elected to the Vice President for the China Power Supply Society in 2013. He has served as the Vice Chair of the Chinese National Steering Committee for College Electric Power Engineering Programs since 2013.

**Shike Wang** received the B.S. degree in electrical engineering from Xi'an Jiaotong University, Xi'an, China, in 2014, where she is currently working toward the Ph.D. degree at the School of Electrical Engineering.

Her current research interests include efficiency optimization of paralleled converters in AC microgrid and distributed generation system.

**Zhiyuan You** received the B.S. and M.S. degrees from Xi'an Jiaotong University, Xi'an, China, in 2011 and 2014, respectively, both in electrical engineering.

He is currently working at NetEase,Inc., Hangzhou, China. His research mainly includes droop control of paralleled converters in AC microgrid.